Available online at www.sciencedirect.com

ScienceDirect

Acta Materialia 90 (2015) 232–241

Acta MATERIALIA

www.elsevier.com/locate/actamat

Extrinsic mechanical size effects in thin ZrNi metallic glass films

M. Ghidelli,[a,b,c,*] S. Gravier,[a] J.-J. Blandin,[a] P. Djemia,[d] F. Mompiou,[e] G. Abadias,[f] J.-P. Raskin[b] and T. Pardoen[c,*]

[a]*Science and Engineering of Materials and Processes, SIMaP, Grenoble University/CNRS, UJF/Grenoble INP, 101 rue de la physique, BP46, 38402 Saint-Martin d'Hères, France*

[b]*Institute of Information and Communication Technologies, Electronics and Applied Mathematics (ICTEAM), Université catholique de Louvain, B-1348 Louvain-la-Neuve, Belgium*

[c]*Institute of Mechanics, Materials and Civil Engineering (IMMC), Université catholique de Louvain, B-1348 Louvain-la-Neuve, Belgium*

[d]*LSPM-CNRS, Université de Paris 13, Sorbonne Paris Cité, F-93430 Villetaneuse, France*

[e]*CEMES-CNRS, Université de Toulouse, 29 rue J. Marvig, 31005 Toulouse, France*

[f]*Institut Pprime, Université de Poitiers-CNRS-ENSMA, Dpt. Physique et Mécanique des Matériaux, SP2MI, Téléport 2, F-86962 Chasseneuil-Futuroscope, France*

Received 9 December 2014; revised 22 February 2015; accepted 23 February 2015

Abstract—Mechanical size effects in Zr_xNi_{100-x} thin metallic glass films are investigated for thicknesses from 200 to 900 nm. Local order, elastic properties and rate sensitivity are shown to be thickness independent, while hardness and fracture resistance are not. The increase of hardness with decreasing thickness is related to the substrate constraint on shear banding. Fracture surfaces exhibit a corrugated morphology, except for thickness below 400 nm exhibiting perfectly flat surfaces. The corrugations appear again on the thinnest films when adding a cap layer, indicating that the fracture mechanisms are primarily dominated by the loading configuration and geometry which constrain the plastic zone extension. Increasing the Ni content from 25% to 58% leads to an increase of elastic modulus, Poisson ratio, strength, activation volume, and fracture toughness. These changes can be understood based on the change in thermodynamic fragility and Zr–Ni bonds formation. $Zr_{75}Ni_{25}$ composition shows exceptionally large rate sensitivity exponent equal to 0.058. The fracture mechanisms are not modified by composition and the fracture toughness is systematically low due to the confinement of the plastic zone.

Keywords: Metallic glasses; Thin films; Size-effects; Mechanical properties; Atomic structure

1. Introduction

The mechanical behavior of bulk metallic glasses (BMGs) has been the subject of intense research for the last 10–20 years [1–4]. Compared with crystalline materials, the liquid-like atomic structure, with no grain boundaries, dislocations, and phase segregations confers BMGs superior mechanical properties involving high fracture strength ($\geqslant$2 GPa) and large elastic deformation (~2%) [1–4]. Nevertheless, the shear band instability phenomenon that occurs during plastic deformation of BMGs – at temperatures below the glass transition temperature (T_g) – leads to a lack of ductility, thus drastically undercutting potential use in structural applications [1–3,5].

One way to overcome the BMGs macroscopic brittle-like behavior is to reduce the dimensions in order to mitigate the catastrophic effects of instabilities on the material behavior and to potentially push the envelop of attainable properties [2,6]. Molecular dynamic simulations [7,8] point toward the existence of a critical length scale required to create "mature" shear bands above 100 nm along the maximum shear direction. Therefore, if the sample size is close to a critical size around 100 nm, the development of a mature shear band may be mitigated or even suppressed, while enhancing mechanical properties such as fracture strength, maximum elastic deformation, and ductility [9–12]. In the case of 200–300 nm-thick ZrCu thin film metallic glasses (TFMGs) under tensile deformation, Tian et al. [9] found a fracture stress close to the theoretical limit with elastic strains above 4%. Other studies have shown that TFMGs are also capable of large plastic deformations

* Corresponding authors at: Institute of Mechanics, Materials and Civil Engineering (IMMC), Université catholique de Louvain, B-1348 Louvain-la-Neuve, Belgium (M. Ghidelli, T. Pardoen); e-mail addresses: matteo.ghidelli@simap.grenoble-inp.fr; thomas.pardoen@uclouvain.be

http://dx.doi.org/10.1016/j.actamat.2015.02.038
1359-6462/

(>10%) and ductile necking [10–12]. Furthermore, mechanical tests on amorphous micro/nanopillars have shown an enhancement of mechanical properties with respect to the bulk counterparts [13,14] and a transition in deformation mode from inhomogeneous (with shear bands formation) to homogeneous has been reported, when the pillar diameter decreases down to 400–500 nm [15]. A thorough review of size effects in amorphous and crystalline materials can be found in Ref. [6]. Obviously, not many applications require structural elements of such small size, but there is a real potential to include them in composite configurations (such as multilayers) or as surface coatings [16].

Although a number of studies have dealt with the mechanical properties of small-volume amorphous samples [6,9–15], the origin of the size effects as well as of the length-scale effects on shear bands formation have not been fully unraveled yet. One possibility is that the change of mechanical properties of TFMGs with respect to bulk counterparts results from a change of atomic arrangement and/or free volume content caused by the different processing routes of TFMGs and BMGs (*intrinsic size effects*), thus reducing the likelihood of pre-existing stress concentrators needed to trigger the formation of shear bands [6,17]. The atomic structure of nano-scale metallic glasses in the form of micropillars and nanotensile specimens could be also altered by focus ion beam (FIB) milling used to shape the test structures. FIB milling can introduce free volume or chemical softening [18], reducing the strength of the metallic glasses. The impact of this heavily disordered glass structure in the FIB-affected surface layer increases as the sample size decreases.

On the other hand, size effects could have an *extrinsic* origin namely due to a geometrical confinement (i.e. film thickness or pillar diameter) [6]. In this regard, Wu et al. [19] have shown that when the specimen size is larger than the critical shear offset necessary for shear bands activation, the deformation is unstable, leading to brittle fracture. On the contrary, specimens smaller than the critical shear offset provide a stable shear deformation allowing the development of extended plasticity in tension. In addition, the loading set-up plays a role in the response of the sample as well as in shear bands stability. It is the case of tapered micropillars [20,21] and the formation of shear bands controlled by the test machine stiffness or by the specimen aspect ratio [2,22,23]. In Ref. [24], we found that the size effect on the fracture behavior of $Zr_{65}Ni_{35}$ TFMGs has an *extrinsic* origin, showing that the failure mechanism and the fracture toughness are thickness dependent even if the film elastic properties – and thus the atomic environment – are comparable with Zr-based BMGs. The low fracture toughness values of ZrNi TFMGs as well as the presence of corrugations on the fracture surface come from the lack of volume available for dissipation and geometrical confinement in TFMGs [24].

The objectives of this work are to investigate the origin of the size effects observed in ZrNi TFMGs deposited on a Si substrate avoiding FIB-milling. The results of the investigation are divided in two main sections. First, we analyze the effect of film thickness – at fixed composition – on local order, elastic properties, nanoindentation hardness, activation volume of the viscoplastic mechanisms, and fracture behavior. Then, we address the effect of the film composition – at fixed thickness – to alter the local order and to observe changes in elastic properties, activation volume, and density as well as in the hardness and fracture behavior.

The choice of a ZrNi binary system was mainly dictated by the wide amorphization range in between 10 and 80 at.% of Zr and by the good resistance to oxidation [25–27]. This avoids crystallization during deposition as well as the formation of a surface oxide which may affect the mechanical response. Moreover, ZrNi BMGs have been the object of several studies highlighting a marked short range order (SRO) favored by strong chemical Zr–Ni interactions [28–30]. Evidences of local order in ZrNi TFMGs have been presented in Ref. [31], in which we analyzed the composition–atomic structure relationship.

The outline of the paper is the following. The deposition of ZrNi TFMGs and the characterization techniques are described in Section 2. Section 3.1 focuses on the results about the effect of thickness – for the amorphous composition $Zr_{65}Ni_{35}$ – on both local order and mechanical properties. Section 3.2 adopts the same strategy – at fixed thickness (800 nm) – to investigate the effect of chemical composition.

2. Experimental

2.1. Thin film deposition and structural characterization

Zr_xNi_{100-x} (at.%) TFMGs have been deposited by DC-magnetron sputtering within a clean room (class 1000) to limit contamination. In order to tune the film composition and to limit the impurity content, a composite sputtering target was designed consisting of pure grade (>99.995%) Ni rectangular slices inserted into a pure (>99.95%) Zr matrix. Additional details on the deposition conditions can be found in Suppl. Data, Fig. S1 and Refs. [31,32].

ZrNi TFMGs have been deposited on a clean Si (100) substrate with different compositions, namely $Zr_{42}Ni_{58}$, $Zr_{65}Ni_{35}$, $Zr_{75}Ni_{25}$, and $Zr_{85}Ni_{15}$ (% at.). A range of thicknesses from 900 down to 200 nm is considered for the composition $Zr_{65}Ni_{35}$, while a thickness equal to 800 nm has been fixed for the three other compositions. The film thickness was measured by both mechanical profilometry and by direct observations using field-emission scanning electron microscope (FE-SEM) after cleavage (see Suppl. Fig. S2). The composition has been checked by FE-SEM with energy dispersive X-ray spectroscopy (EDX) and with electron probe micro analysis (EPMA) and found to be constant over the Si substrate with the absence of impurities (see Suppl. data Table S1). The atomic structure has been characterized by grazing incidence X-ray diffraction (GIXRD, Cu Kα radiation) and by transmission electron microscopy (TEM), while the mass density ρ has been extracted from X-ray reflectivity (XRR) technique, see Suppl. Data and Refs. [31,32].

A 450 nm-thick SiO_2 layer has been deposited onto a 400 nm-thick $Zr_{65}Ni_{35}$ film to investigate the possible impact of the fracture behavior by changing the constraint on the plastic flow and the stress state compared with the same film thickness involving a free surface. The SiO_2 film has been deposited by DC-magnetron sputtering immediately after the deposition of the ZrNi film. The parameters used for the deposition of the SiO_2 are reported in the Suppl. Data.

2.2. Mechanical characterization of ZrNi TFMGs

2.2.1. Surface Brillouin spectroscopy

Surface Brillouin spectroscopy (SBS) has been used to extract the elastic constants. The SBS measurements have been carried out with a monochromatic laser ($\lambda = 532$ nm) to probe the thermally excited acoustic waves generated inside the sample. The scattered light has been collected using a backscattering geometry. The SBS spectra were obtained at room temperature in air using a naturally p-polarized light, with typical acquisition times of 2 h and 200–300 mW power. For nearly opaque layers – such as ZrNi films – the scattering mechanism is restricted to the scattering of light by acoustic waves traveling parallel to the film plane [33]. For films with thicknesses around the acoustic wavelength (~0.3 μm) and deposited on a substrate with higher acoustic phase velocity ("slow" film on "fast" substrate), the surface acoustic waves consist of the Rayleigh wave (R) and the so-called Sezawa guided waves (S_1–S_n) at higher frequencies [33]. The SBS spectra for $Zr_{65}Ni_{35}$ 200 and 900-nm thick films are reported in the Suppl. data, Fig. S5. The velocity of the Rayleigh surface wave (v_R) is mainly dependent on the transverse velocity (v_T) [34] through the relation $v_R = \beta v_R$ where β is slightly dependent upon the different elastic constants. TFMGs have been considered isotropic [1,3] with two independent elastic constants (longitudinal C_{11} and transverse C_{44}). The elastic constants $C_{11} = v_l^2\rho$ and $C_{44} = v_T^2\rho$ have been calculated after measuring the longitudinal v_l and transverse v_T acoustic wave propagation velocities, and film density ρ (XRR). The elastic constants are then combined to determine the elastic modulus (E) and the Poisson ratio (v) through:

$$E = \frac{C_{44}(3C_{11} - 4C_{44})}{C_{11} - C_{44}} \quad \text{and} \quad v = \frac{C_{11} - 2C_{44}}{2(C_{11} - C_{44})} \tag{1}$$

2.2.2. Nanoindentation

Indentation tests were made with a diamond Berkovich tip mounted on an Agilent G200 Nanoindenter DCM II head. Prior to testing, the tip area function was calibrated using a fused silica reference. The nanoindentation measurements were performed under load-control mode at room temperature using the continuous stiffness measurements (CSM) method providing the current value of hardness with increasing indentation depth. The allowable thermal drift rate has been limited to 0.05 nm s^{-1}. Sixteen indents were performed in each sample. The maximum indentation depth was fixed at 500 nm for film thickness larger than 500 nm. The load rate ($\dot{P}/P$) was imposed equal to 0.05 s^{-1}. The hardness was calculated using the Oliver and Pharr method [35].

The activation volume of ZrNi TFMGs can be estimated using nanoindentation data based on the method proposed by Pan et al. [36]. In BMGs, the constitutive law that controls the viscoplastic deformation is assumed to follow an Arrhenius kinetics of the form $\dot{\gamma} = \dot{\gamma}_s \exp(-\Delta G/kT)$ where $\dot{\gamma}$ is the strain rate, $\dot{\gamma}_s$ is a constant, ΔG is the activation free energy for the elementary deformation mechanism, k is the Boltzmann constant, and T is the temperature [3]. ΔG is related to the applied shear stress τ and temperature as:

$$d\Delta G = \left(\frac{\partial \Delta G}{\partial \tau}\right)_T d\tau + \left(\frac{\partial \Delta G}{\partial T}\right)_\tau dT = -\Delta V d\tau - \Delta S dT. \tag{2}$$

Neglecting entropy variation ($\Delta S \approx 0$), the so called (apparent) activation volume (ΔV) is given by:

$$\Delta V = -\left(\frac{\partial \Delta G}{\partial \tau}\right)_T = \frac{kT}{\tau}\left(\frac{\partial \ln \dot{\gamma}}{\partial \ln \tau}\right)_T. \tag{3}$$

The strain rate sensitivity is defined as $m = (\partial \ln \tau / \partial \ln \dot{\gamma})_T$, hence $\Delta V = \frac{kT}{m\tau}$. Moreover, if the hardness (H) is considered to be equal to $3\sigma_y \approx 3\sqrt{3}\tau_y$ [3,36,37], one gets:

$$\Delta V \approx \frac{3\sqrt{3}kT}{mH}. \tag{4}$$

Note that the assumption $H \approx 3\sigma_y$ is strictly valid only if metallic glass yielding can be described by von Mises criterion [36,37]. This relationship provides thus only an approximation of the yield stress and the result should be considered as an upper limit. More sophisticated models based on a Mohr–Coulomb yield criterion provide a more exact relationship between H and σ_y [38].

Therefore, the activation volume can be extracted by knowing the strain rate sensitivity (m) and the hardness (H). The rate sensitivity m can be calculated using $\partial \ln H / \partial \ln \dot{\varepsilon}$ where $\dot{\varepsilon}$ is the representative indentation strain rate [3,36,37]. This strain rate can be estimated as equal to $\dot{P}/2P$ where $\dot{P}/P$ is the (constant) loading rate [36]. Three different loading rates equal to 0.02, 0.05, and 0.1 s^{-1} have been used.

2.2.3. Fracture tests

Fracture analysis was performed by cracking the backside of the Si wafer from a shallow notch induced by a diamond tip, with the crack eventually propagating into the ZrNi TFMGs. The fracture surfaces are observed by FE-SEM. More details about the method are reported in [24]. Here, we used the same method to analyze the fracture behavior of different compositions of ZrNi TFMGs as well as the effect of a SiO_2 capping layer.

3. Results and discussion

3.1. Thickness effect at constant composition

The mechanical behavior of the composition $Zr_{65}Ni_{35}$ (at.%) is studied first. We investigated a range of thicknesses from 200 nm up to 900 nm in which size-effects are expected [9,13–15,20]. When the sample sizes are extremely small (⩽100 nm) major influence from surface conditions can play a role [9], thus making difficult a direct comparison with bulk specimens.

In this section, we perform a structural characterization of $Zr_{65}Ni_{35}$ for different thicknesses followed by the analysis of the elastoplastic and fracture behavior.

3.1.1. Structural characterization

The GIXRD diffractograms corresponding to $Zr_{65}Ni_{35}$ TFMGs are reported in Fig. 1a for the different thicknesses. All specimens exhibit a fully amorphous structure as can be noticed by the presence of an asymmetric first sharp diffraction peak (FSDP) followed by a broader halo at higher

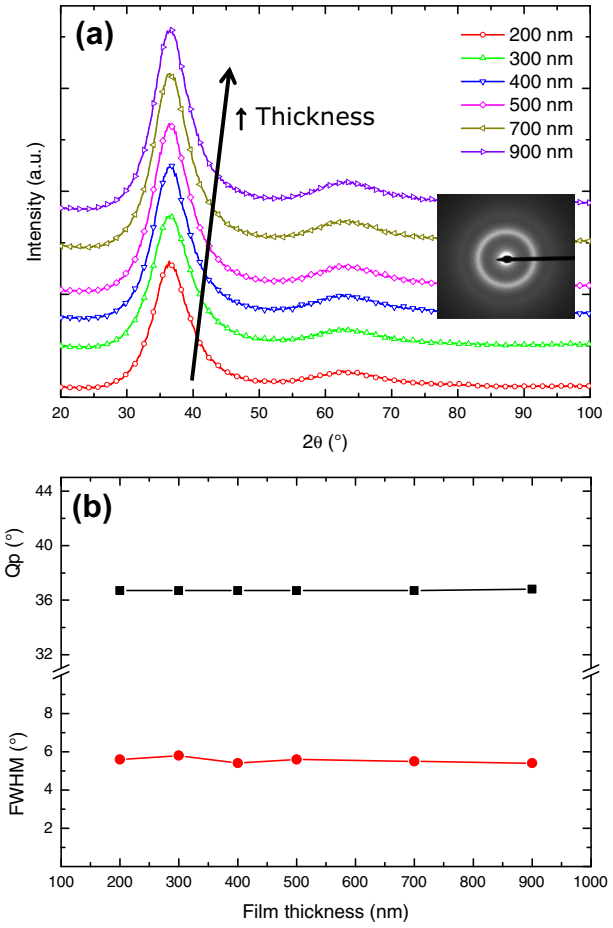

Fig. 1. GIXRD diffractograms for $Zr_{65}Ni_{35}$ TFMGs with different thicknesses. (a) A first sharp diffraction peak (FSDP) and a second broader halos are observed, diffractograms are vertical shifted for sake of clarity. In the inset, TEM microdiffraction pattern for the 900 nm-thick film showing two diffuse halos, further proving the film's amorphous structure. (b) FSDP (Q_p) and full width at half maximum (FWHM) extracted from GIXRD diffractogram in (a). Both quantities are thickness independent and respectively around 36.7° and 5.5°.

angles. This is confirmed by the absence of crystalline spots in the 900 nm-thick specimen analyzed by TEM microdiffraction (see inset of Fig. 1a). The position of the FSDP Q_p and the full width at half maximum (FWHM) – obtained after fitting with a Lorentzian function – are constant and equal to 36.7° and 5.5°, respectively (Fig. 1b). The average atomic spacing is close to 2.4 Å. If the diffractograms in Fig. 1a are converted into scattering vector (q, $Å^{-1}$) coordinates by means of $q = 4\pi \sin\ \theta/\lambda$, where λ is the X-ray wavelength (1.5418 Å), the FWHM is equal to 0.39 $Å^{-1}$ slightly below the literature values for BMGs (~0.5 $Å^{-1}$) [39]. The thickness independent values of both Q_p and FWHM indicate that all specimens involve a similar atomic structure (or the same free volume content). Moreover, they show the same strong Zr–Ni atomic correlations – as expected for the compositions close to $Zr_{65}Ni_{35}$ [28,30,31] – with the FWHM below the literature values reported for multicomponent highly disordered BMGs [39].

3.1.2. Elastoviscoplastic properties

The elastic modulus (E) and Poisson ratio (v) of TFMGs are calculated by using Eq. (1) after combining the elastic constants C_{11} and C_{44} extracted by means of surface Brillouin spectroscopy (SBS). Both C_{11} and C_{44} are thickness independent (see Fig. S6 in the Suppl. Data), thus providing constant values of E and v, respectively around 72 GPa and 0.39 (Fig. 2). These results can be compared with the literature values for ZrNi ribbons with a similar composition which report an elastic modulus around 62 GPa and a Poisson ratio of 0.375 [27,40]. The thickness independence of the values of E and v further proves that the films involve the same atomic structure.

The variation of hardness (H) as a function of indentation depth is reported in Fig. 3a and b for the different film thicknesses. After an initial jump at very low indentation depth presumably due to the surface–tip interaction, the hardness slightly increases with decreasing film thickness irrespective of the selected penetration depth (Fig. 3a). A similar trend is found if H is plotted against the normalized indentation depth, namely the ratio between the indentation depth and film thickness (see Suppl. data, Fig. S8). If an average value of hardness is extracted from the normalized indentation depth between 10% and 20%, the hardness is found to increase from 6.3 GPa for a 900 nm-thick film up to 7.3 GPa for a 200 nm-thick film (Fig. 3b). Note that Ristić et al. [40] reported a micro-hardness of 5.2 GPa for $Zr_{65}Ni_{35}$ ribbons. The yield strength σ_y, taken equal to $H/3$ as a first approximation [3], increases from 2.1 up to 2.4 GPa for thicknesses varying from 900 to 200 nm, which is a range consistent with published Zr-based BMGs values [41]. The moderate increase of hardness with decreasing film thickness irrespective of the indentation depth and of the normalized indentation depth as well cannot be explained on the basis of a change in atomic arrangement which we have shown to be thickness independent, and it should thus have an *extrinsic* origin. The most obvious explanation is a substrate confinement effect on the development of the shear bands (SBs). This phenomenon is quite similar to a compression test on an amorphous bulk specimens having a low aspect ratio (height to diameter). In this case, SBs are often generated at the contact interface between the sample and the machine cross-head, and the confinement effect prevents the free glide needed to create the shear offset [2,42]. The low aspect ratio also favors the formation of multiple SBs, *apparently* enhancing the measured strength of the sample [2]. Even if the exact load conditions under the indent tip are different with respect to

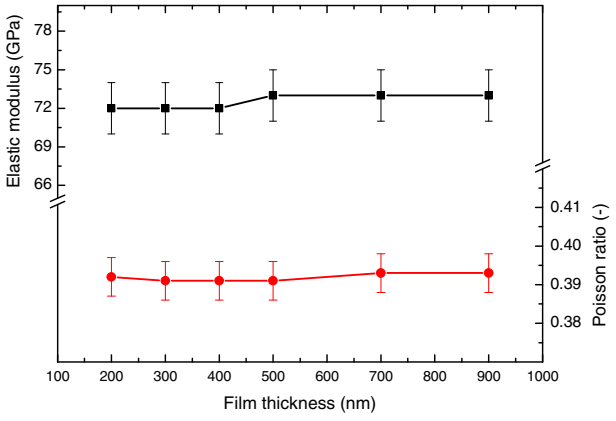

Fig. 2. Thickness dependence of elastic modulus (E) and Poisson ratio v measured by surface Brillouin spectroscopy (SBS). The E and v values are constant and equal to 72 GPa and 0.39, respectively.

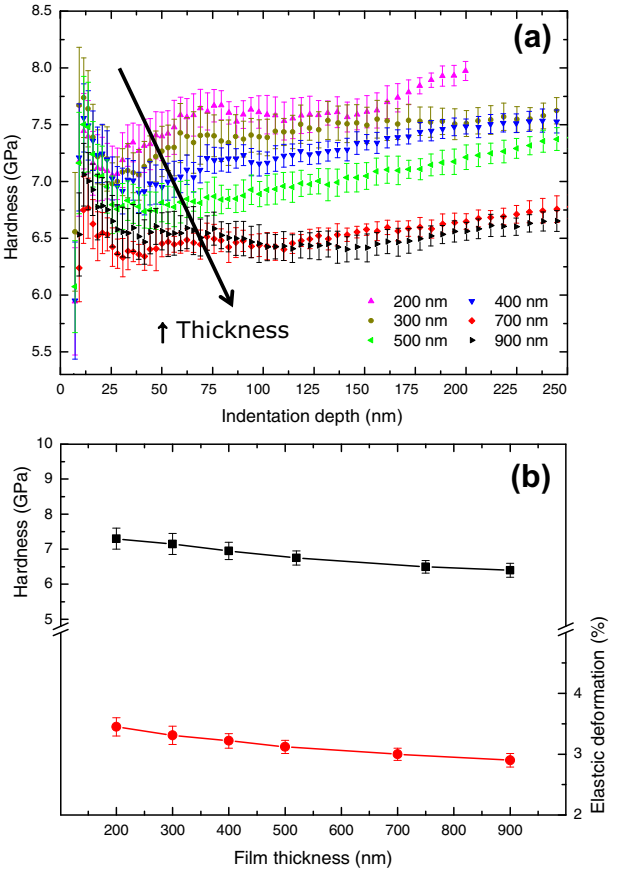

Fig. 3. Nanoindentation results. (a) Continuous stiffness measurement (CSM) hardness as function of the indentation depth. (b) Average hardness as function of film thickness. The hardness is determined for a normalized indentation depth (i.e. ratio between indentation depth and film thickness) between 10% and 20%.

a compression test, the confinement effect is enhanced for small thicknesses, thus potentially affecting the nucleation processes of SBs. The local constraint favors SBs nucleation to accommodate the deformation induced by the indent. Fig. 3b shows also the variation of $H/3E$ which quantifies the elastic strain at yielding. The elastic strain is around 3% which is near the theoretical value of 2.7% [43].

Fig. 4 shows the variation of H with strain rate for different film thicknesses. The variations of H as a function of the normalized indentation depth for different strain rates and thicknesses are reported in the Suppl. data as Fig. S9a and b. Once again the hardness clearly increases with decreasing film thickness at all strain rates, thus confirming the results of Fig. 3. The hardness increases with increasing the imposed strain rate. This phenomenon is described also for BMGs and it is mainly related to the thermal activation mechanism of the nucleation of SBs [3,44]. The extracted rate sensitivity coefficient (m) is independent of thickness and equal to ~0.026. The activation volume calculated for the 700 and 900 nm-thick specimens – which exhibit very close hardness values – is around 120 Å^3. These values of m are comparable with the literature values for Zr-based BMGs having m equal to 0.021 for a $Zr_{44}Cu_{44}Al_6Ag_6$ BMG [36]. These values are larger than in other families of BMGs usually showing values smaller than 0.01 [36]. BMGs are made of different sizes

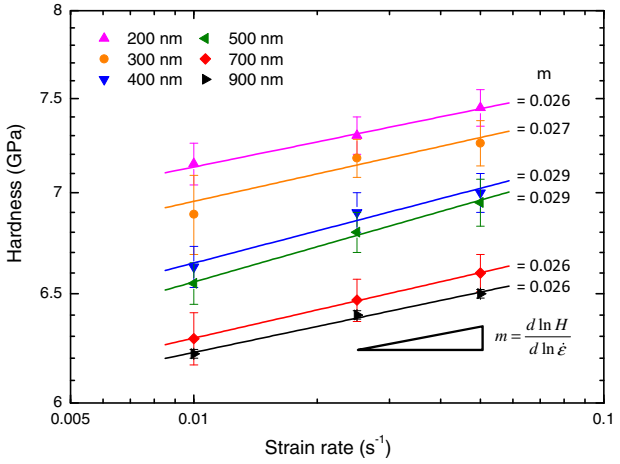

Fig. 4. Determination of the rate sensitivity of hardness (m) for $Zr_{65}Ni_{35}$ TFMGs with different thicknesses. The m values are constant whatever the thickness and equal to 0.026.

of elementary atoms and they are produced from liquid phase techniques [17], thus leading to different atomic organizations affecting the barrier for triggering SBs [36,45]. The values of the activation volume as a function of composition are further discussed in Section 3.2.2.

3.1.3. Fracture behavior

The fracture behavior of the TFMGs has been analyzed in a recent previous study in which we reported a transition in fracture mechanism from corrugated to mirror-like, when the film thickness is below a 500 nm threshold, see Ref. [24]. Finite element simulations have shown that *plastic collapse* – namely the merging between the plastic zones ahead the crack tip and the opposite one due to the bending configuration – occurs for small thicknesses (⩽400 nm) preventing the cavitation and/or meniscus instability to develop and leading to a mirror-like surface such as in Fig. 5a. We showed that the fracture behavior is intimately

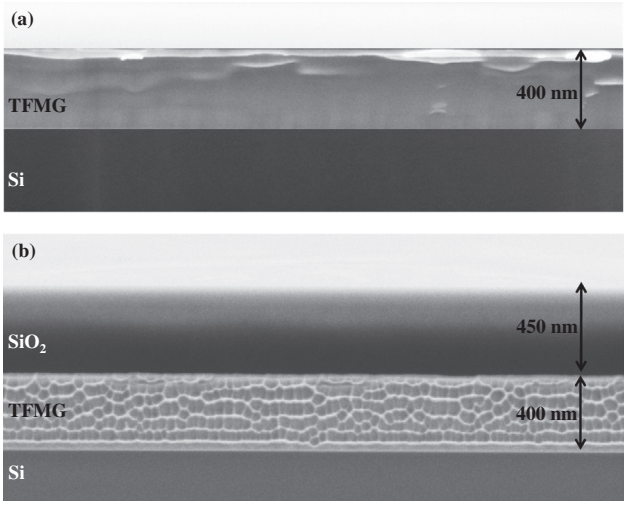

Fig. 5. SEM micrographs of fracture surfaces for $Zr_{65}Ni_{35}$ TFMGs. (a) A mirror-like fracture surface is present for a 400 nm-thick because of the plastic collapse of plastic zones ahead the crack tip and due to bending configuration. (b) A corrugation pattern appears for a 400 nm-thick $Zr_{65}Ni_{35}$ film if it is coated by a SiO_2 cap layer since the bending plastic zone is moved in the SiO_2 layer.

related to thickness confinement. In order to confirm this claim, we deposited in the present study a SiO_2 cap layer onto the TFMGs aiming to alter the fracture morphology by translating the compression zone within the SiO_2 in order to analyze possible changes in the fracture behavior of TFMGs. The fracture surface of a 400-nm thick $Zr_{65}Ni_{35}$ TFMGs coated with a 450 nm SiO_2 layer is shown in Fig. 5b demonstrating the presence of a corrugated pattern with an average width (w) of ~38 nm, very close to the size exhibited by a 520 nm-thick film reported in [24]. The same 400-nm TFMG without SiO_2 capping did not show any corrugation but a flat mirror-like surface (Fig. 5a). As expected, this abrupt change comes from the fact that the compressive zone due to bending lies in the SiO_2 layer, thus allowing the hydrostatic stress peak to develop over a region of the ZrNi film large enough for triggering a cavitation mechanism responsible for the observed corrugation pattern. In Ref. [24], we have shown by finite element simulations that the magnitude of the hydrostatic stress gradient is equal to $55{\cdot}10^3$ GPa/mm, for a thickness range from 300 up to 900 nm. This extremely high value comes from the strong geometrical confinement which prevents the meniscus instability to develop and which leads to cavitation and formation of corrugations, see Ref. [24] for more details. This proves again that the fracture mechanisms and the length scale over which they take place are dictated by extrinsic factors related to the loading configuration and external dimensions that set the constraint on the plastic zone size and on the magnitude of the stresses attained in the fracture process zone. The fracture toughness (K_c) calculated as [24,46]:

$$K_c = \sigma_y\sqrt{40w} \tag{5}$$

is equal to 2.7 MPa $m^{1/2}$ well below the expected value around 50 MPa $m^{1/2}$ estimated from a Poisson ratio of 0.39 for a BMG (Fig. 2) [47], but in agreement with results we obtained for TFMGs, Ref. [24]. As explained above, this low toughness is not a result of a particular atomic structure or of an intrinsic length scale effect on the mechanisms but of the restriction on the plastic zone development due to the bending configuration and small thickness. This restriction on the plastic zone development is somewhat analogous to the substrate effect affecting the apparent hardness in nanoindentation tests.

3.2. Composition effect at constant thickness

The effect of composition on local order, elastoplastic properties, and fracture behavior have been studied for different Zr_xNi_{100-x} (at.%) TFMGs with x equal to 42, 75 and 85 at fixed thickness of 800 nm. We first present the structural characterization followed by the mechanical behavior in order to understand the origin of size-effects and how composition can influence local order and the macroscopic properties.

3.2.1. Structural analysis of Zr_xNi_{100-x} TFMGs

Cross-section TEM micrographs reported in Fig. 6a–c show the microstructural evolution in ZrNi TFMGs when changing the percentage of Zr. In particular, small nanocrystals (~3 nm) can be observed for $Zr_{75}Ni_{25}$ (Fig. 6b), while intense crystallization occurred for $Zr_{85}Ni_{15}$ in which 60–70 nm-long α-Zr crystallites are embedded in an amorphous matrix (Fig. 6c), Ref. [31].

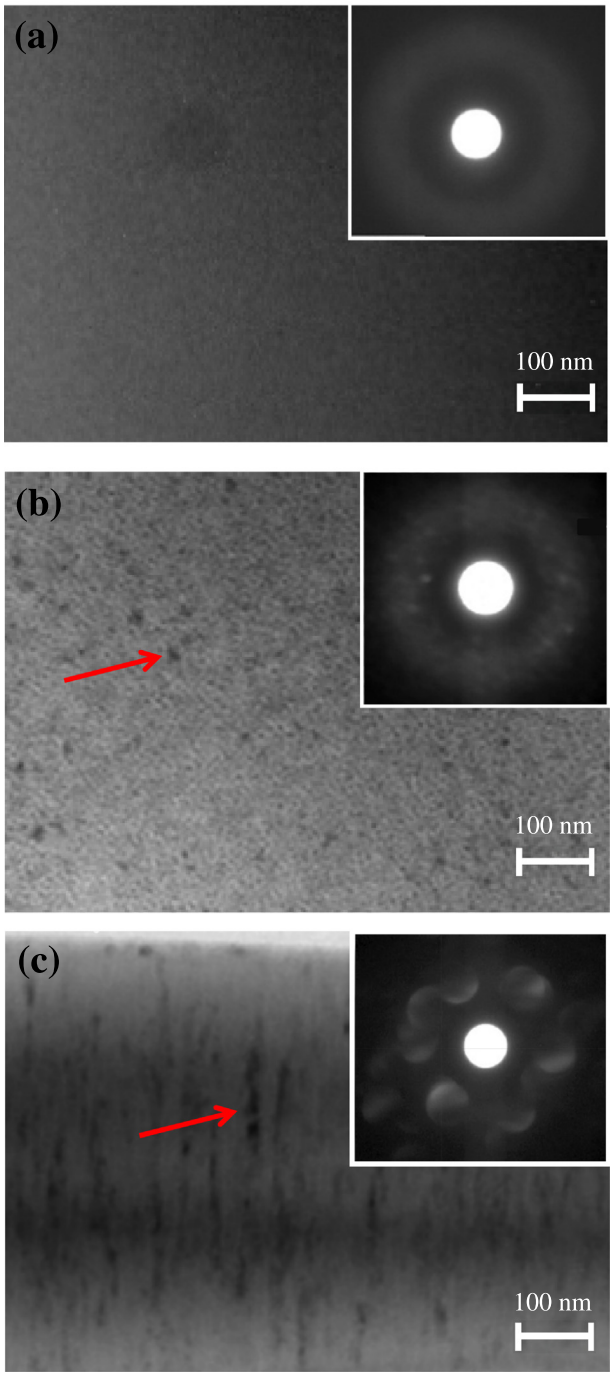

Fig. 6. Cross-section TEM images of Zr_xNi_{100-x} TFMGs with a thicknesses equal to 800 nm. In the inset, the microdiffraction pattern. From (a) to (c) the composition $Zr_{42}Ni_{58}$, $Zr_{75}Ni_{25}$, and $Zr_{85}Ni_{15}$, respectively. The red arrows indicate dispersed nanocrystals of around 3 nm and 60 nm-long, respectively for $Zr_{75}Ni_{25}$ and $Zr_{85}Ni_{15}$. (For interpretation of the references to colour in this figure legend, the reader is referred to the web version of this article.)

The crystalline phase is oriented normal to the Si surface and uniformly distributed within the film as confirmed by XRD experiments reported in Ref. [31]. On the other hand, the structure of $Zr_{42}Ni_{58}$ is fully amorphous as proven by the absence of crystalline spots in the microdiffraction pattern (Fig. 6a). In Ref. [31], we have discussed the structure of the crystalline phase as well as

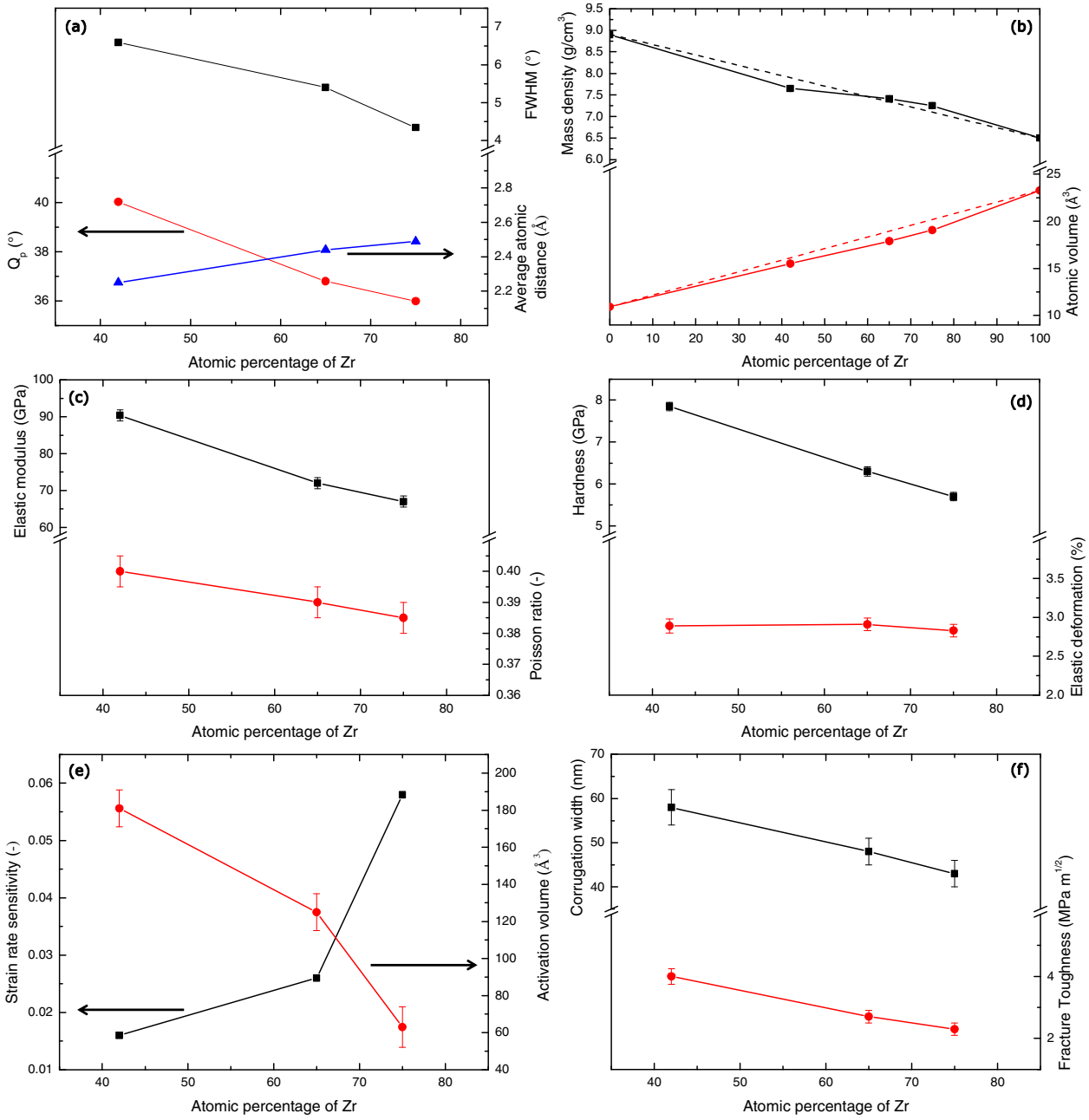

Fig. 7. Variation of the different physical and mechanical characteristics as a function of film composition: (a) position and FWHM of the first sharp diffraction peak (FSDP, Q_p) – the average atomic spacing decreases when increasing the Zr content in the film, indicating the formation of hetero Zr–Ni bonds; (b) mass density measured by X-ray reflectivity (XRR) – the values follow a mixing rule obtained from crystalline Zr and Ni (dashed lines). An error bar of ± 0.04 g/cm^3 is added, but it is not distinguished from the data set; (c) elastic modulus and Poisson ratio measured by surface Brillouin spectroscopy (SBS); (d) nanoindentation hardness and elastic strain at yielding; (e) activation volume and rate sensitivity exponent; (f) corrugation size and fracture toughness.

its origin in terms of a reduced mixing enthalpy for Zr-rich specimens. Here, we point out that the composition induces a significant change in film structure altering the local order of the amorphous phase as well. Since the aim of the paper is to investigate the origin of size-effects in TFMGs, we exclude from the following analyses $Zr_{85}Ni_{15}$ films which show intense crystallization, while still considering the composition $Zr_{75}Ni_{25}$ due to the low percentage and size of the crystallites which are not detectable with the GIXRD, see also Suppl. Fig. S3.

The evolution of the position of the FSDP (Q_p) and FWHM as a function of film composition is reported in Fig. 7a. Both Q_p and FWHM increase if the percentage of Zr decreases. In Ref. [31], we have shown that the trend of Q_p is the same as for ZrNi ribbons [26] having different compositions and mainly related to the ease of formation of Zr–Ni bonds for Ni-rich specimens. This leads to a reduction of the average atomic distances caused by the different atomic radius of Ni and Zr atoms, respectively 135 and 155 pm (see Fig. 7a). The increment of FWHM when

reducing the Zr concentration is due to the highly disordered structure favored by the high mixing enthalpy contribution for the composition $Zr_{42}Ni_{58}$ [25,31]. Anyway, the converted scattering vector values of FWHM are still below the characteristic value of 0.5 $Å^{-1}$ for a multicomponent BMG [39], again indicating strong Zr–Ni interactions [28,29].

Fig. 7b shows the variation of the mass density (ρ) and of the atomic volume as a function of Zr concentration (the XRR scans are reported in the Suppl. Data Fig. S4). The atomic volume for amorphous alloys is defined as $V_a = \bar{A}/\rho N_a$, where $\bar{A}$ is the weighted atomic mass and N_a is Avogadro's number [39,48]. The atomic volume decreases when reducing the percentage of Zr due to the favored formation of strong Zr–Ni bonds. The mass density and the atomic volume follow a mixing rule (dashed lines in Fig. 7b) obtained from crystalline Zr and Ni. The Ni density is higher than Zr, respectively equal to 8.91 and 6.50 g/cm^3 leading to a reduced atomic volume respectively of 10.93 $Å^3$ and of 23.28 $Å^3$ as reported in Ref. [48]. All the specimens have an atomic volume comparable to ZrNi ribbons with similar composition [39,48].

3.2.2. Elastoviscoplastic properties of Zr_xNi_{100-x} TFMGs

The effect of composition on the elastic modulus (E) and Poisson ratio (v) is displayed in Fig. 7c. The evolution of C_{11} and C_{44} is reported in the Suppl. Fig. S7. There is a marked effect on the elastic modulus which increases from 65 GPa up to 91 GPa when decreasing the Zr content, while v slightly increases reaching the value of 0.4 for $Zr_{42}Ni_{58}$. The values of E and v are slightly above the literature values reported in Refs. [27,40]. The composition could significantly modify the film local order, enhancing the formation of Zr–Ni bonds when reducing the Zr content in the film. This trend is consistent with the reported evolution of Q_p and atomic volume in Fig. 7a and b.

The hardness increases with decreasing Zr content from 5.6 GPa for $Zr_{75}Ni_{25}$ up to 7.8 GPa for $Zr_{42}Ni_{58}$ (Fig. 7d). Contrary to what appears in Fig. 3, this trend is attributed to a change of local order due to the presence of strong Zr–Ni bonds when reducing the Zr content. We further note that these values are in agreement with the literature results using the following approximate relationship $\sigma_y = H/3$ [40,41]. Fig. 7d shows that the elastic strain at yielding estimated by $H/3E$ is around 2.8% for all compositions, very close to the theoretical value.

The variation of activation volume as a function of film composition is shown in Fig. 7e. There is a large effect when reducing the Zr content which leads to an increase of the activation volume up to 180 $Å^3$ for $Zr_{42}Ni_{58}$, while $Zr_{75}Ni_{25}$ exhibits a very small value of about 60 $Å^3$. This evolution reflects into the strain rate sensitivity coefficient (m) which is equal to 0.016 and 0.058, respectively for $Zr_{42}Ni_{58}$ and $Zr_{75}Ni_{25}$ (see Suppl. Fig. S10). In the case of $Zr_{42}Ni_{58}$ this value is in agreement with results reported in [36]. The value $m = 0.058$ is larger than any other value found in the literature. The largest value we have found is in Ref. [49] with $m = 0.05$ for $Pd_{77}Si_{23}$ 5.5 μm-thick film from which micropillars have been machined and compressed. This particularly large rate sensitivity is intriguing and deserves further investigation.

When reducing the Zr percentage, Zr–Ni bonds are favored leading to the increase of mass density, elastic modulus, hardness and a reduction of average atomic distances. The increase of the apparent activation volume is rather indicative of a structural heterogeneity characterized by large loosely packed regions (STZs) – due to the enhanced mixed entropy. This result is intimately related with the enhanced FWHM for $Zr_{42}Ni_{58}$ (Fig. 7a). A better plasticity is expected for Zr-rich specimens showing an higher rate sensitivity, a lower activation volume, and less strong atomic bonds, which promote the nucleation and formation of multiple shear bands, thus enhancing mechanical properties [36,45].

3.2.3. Fracture behavior of Zr_xNi_{100-x} TFMGs

Fig. 8 shows the fracture surfaces corresponding to the different TFMG compositions. All films exhibit a corrugation pattern which covers approximately 3/4 of the film thickness leaving a smooth top region, so-called

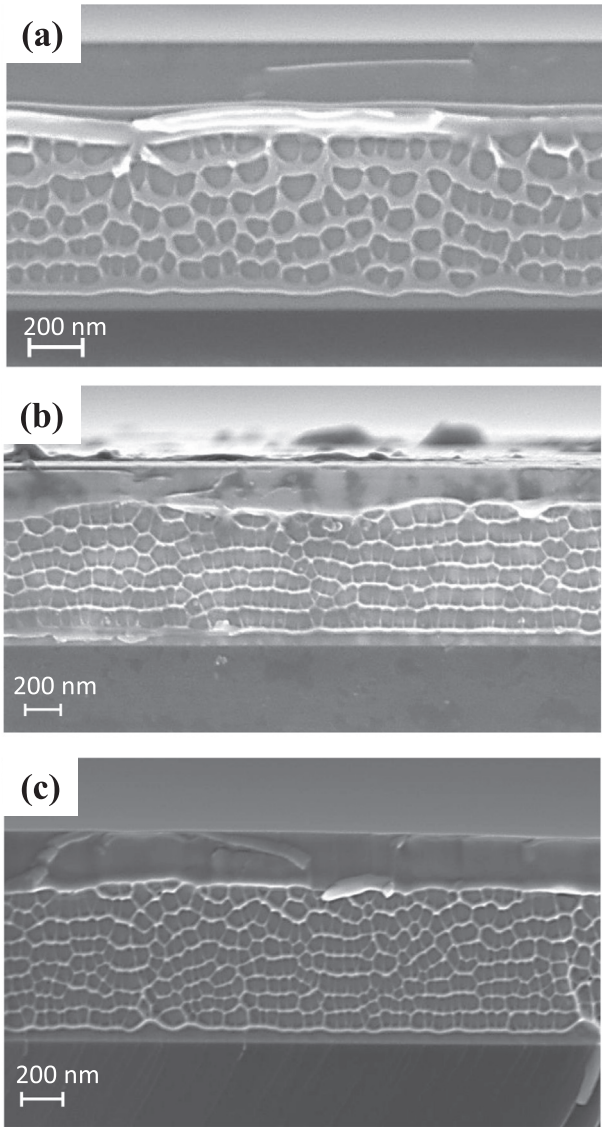

Fig. 8. SEM micrographs of fracture surfaces for Zr_xNi_{100-x} TFMGs with a thickness of 800 nm. From (a) to (c) the compositions $Zr_{42}Ni_{58}$, $Zr_{65}Ni_{35}$, $Zr_{75}Ni_{25}$, respectively. All fracture surfaces show a corrugated pattern. The corrugation size increases when reducing the Zr content in the film, while folded layer on top surfaces is always present. The composition $Zr_{42}Ni_{58}$ (a) clearly shows a different morphology.

"folded layer" Ref. [24]. These phenomena have been already discussed in Section 3.1.3 and in Ref. [24] and related to cavitation and to the frustration of the meniscus instability mechanism. The ensuring plastic collapse between the fracture process zone (FPZ) ahead of the propagating crack tip and the compressive region caused by the bending leads to the formation of the folded layer. Fig. 8 confirms that the mechanisms are globally the same for the different compositions: the $Zr_{65}Ni_{35}$ and $Zr_{75}Ni_{25}$ show essentially a similar corrugation morphology. The $Zr_{42}Ni_{58}$ exhibits larger corrugations which are more reminiscent of the formation of a liquid layer dictating the process of cracking by a meniscus instability propagation [24]. This agrees with the more liquid-like character of this composition. The average corrugation width (w) increases from 43 nm up to 58 nm when reducing the Zr content, thus leading to a change in fracture toughness from 2.3 MPa $m^{1/2}$ up to 4.0 MPa $m^{1/2}$, based on the use of Eq. (5), see Fig. 7f. Therefore, this further proves that the fracture toughness and the size of the corrugations are primarily set by the constraint on plastic flow development, see Section 3.1.3 and Ref. [24].

4. Conclusion

The dependence of the mechanical properties of ZrNi thin film metallic glasses (TFMGs) upon film thickness and composition has been investigated by combining characterization and mechanical testing. The main conclusions of the study are the following:

- For the amorphous composition $Zr_{65}Ni_{35}$, the local order, the elastic properties and the activation volume are thickness independent, while the nanoindentation hardness and the fracture mechanisms show a variation directly related to the constraint imposed by the geometry and by the loading configuration on the development of the plastic zone. The hardness increases when decreasing the thickness. An abrupt transition on the fracture surface from mirror-like to corrugations is observed if a SiO_2 cap layer is deposited on the very thin TFMGs. The cap layer shifts the compressive plastic zone due to bending geometry outside the TFMG allowing the peak hydrostatic stress to spread over a region sufficiently large to generate a cavitation mechanism.
- A change of film composition at fixed thickness (800 nm) involves a change of fracture morphology and of nanoindentation hardness, but also of the local atomic environment in terms of elastic properties, mass density, activation volume, position and amplitude of diffracted halos. All compositions involve elastic strains at yielding very close to the theoretical value of 2.7%. The Ni-rich films are characterized by the formation of strong Zr–Ni bonds as well as by larger activation volumes. The Zr-rich films show very large rate sensitivity $m = 0.058$ larger than all the values found in the literature.

The present study confirms previous findings in Ref. [24] showing that size effects on hardness and fracture mechanisms for thin metallic glass films have an *extrinsic* origin related to a thickness confinement of plasticity instead of a change in atomic arrangement. Size effects with an *intrinsic* origin are not observed within this study, except, perhaps regarding the very large rate sensitivity which requires further investigations.

Acknowledgments

This work has been funded by the Belgian Science Policy through the IAP 7/21 project. We acknowledge Audrey Favache for the help with the nanoindentation tests, IDS-FunMat for the PhD financial support and the PTA (Plateforme Technologique Amont) in Grenoble (France) for deposition facilities.

Appendix A. Supplementary data

Supplementary data associated with this article can be found, in the online version, at http://dx.doi.org/10.1016/j.actamat.2015.02.038.

References

[1] M. Ashby, A. Greer, Scr. Mater. 54 (2006) 321.
[2] A.L. Greer, Y.Q. Cheng, E. Ma, Mater. Sci. Eng. R 74 (2013) 71.
[3] C.A. Schuh, T.C. Hufnagel, U. Ramamurty, Acta Mater. 55 (2007) 4067.
[4] M. Telford, Mater. Today 7 (2004) 36.
[5] Y. Zhang, A.L. Greer, Appl. Phys. Lett. 89 (2006) 071907.
[6] J.R. Greer, J.T.M. De Hosson, Prog. Mater. Sci. 56 (2011) 654.
[7] A.J. Cao, Y.Q. Cheng, E. Ma, Acta Mater. 57 (2009) 5146.
[8] F. Shimizu, S. Ogata, J. Li, Acta Mater. 54 (2006) 4293.
[9] L. Tian, Y.Q. Cheng, Z.W. Shan, J. Li, C.C. Wang, X.D. Han, J. Sun, E. Ma, Nat. Commun. 3 (609) (2012) 1.
[10] L. Tian, Z.-W. Shan, E. Ma, Acta Mater. 61 (2013) 4823.
[11] Q. Deng, Y. Cheng, Y. Yue, L. Zhang, Z. Zhang, X. Han, E. Ma, Acta Mater. 59 (2011) 6511.
[12] H. Guo, P.F. Yan, Y.B. Wang, J. Tan, Z.F. Zhang, M.L. Sui, E. Ma, Nat. Mater. 6 (2007) 735.
[13] C.J. Lee, J.C. Huang, T.G. Nieh, Appl. Phys. Lett. 91 (2007) 161913.
[14] D. Jang, J.R. Greer, Nat. Mater. 9 (2010) 215.
[15] C.A. Volkert, A. Donohue, F. Spaepen, J. Appl. Phys. 103 (2008) 083539.
[16] J.P. Chu, J.S.C. Jang, J.C. Huang, H.S. Chou, Y. Yang, J.C. Ye, Y.C. Wang, J.W. Lee, F.X. Liu, P.K. Liaw, Y.C. Chen, C.M. Lee, C.L. Li, C. Rullyani, Thin Solid Films 520 (2012) 5097.
[17] S. Singh, M.D. Ediger, J.J. de Pablo, Nat. Mater. 12 (2013) 139.
[18] Y.H. Liu, F. Zhao, Y.L. Li, M.W. Chen, J. Appl. Phys. 112 (2012) 063504.
[19] F.F. Wu, Z.F. Zhang, S.X. Mao, Acta Mater. 57 (2009) 257.
[20] M.C. Liu, J.C. Huang, K.W. Chen, J.F. Lin, W.D. Li, Y.F. Gao, T.G. Nieh, Scr. Mater. 66 (2012) 817.
[21] X.L. Wu, Y.Z. Guo, Q. Wei, W.H. Wang, Acta Mater. 57 (2009) 3563.
[22] Y. Yang, C.T. Liu, J. Mater. Sci. 47 (2011) 55.
[23] Z. Han, W.F. Wu, Y. Li, Y.J. Wei, H.J. Gao, Acta Mater. 57 (2009) 1367.
[24] M. Ghidelli, S. Gravier, J.-J. Blandin, J.-P. Raskin, F. Lani, T. Pardoen, Scr. Mater. 89 (2014) 9.
[25] A.I. Zaitsev, N.E. Zaitseva, E.K. Shakhpazova, A.A. Kodentsov, Phys. Chem. Chem. Phys. 4 (2002) 6047.
[26] K.H.J. Buschow, N.M. Beekmans, Phys. Rev. B Condens. Matter 19 (1979) 3843.
[27] Y.D. Dong, G. Gregan, M.G. Scott, J. Non-Cryst. Solids 43 (1981) 403.
[28] X.J. Liu, X.D. Hui, G.L. Chen, T. Liu, Phys. Lett. A 373 (2009) 2488.
[29] T. Fukunaga, K. Itoh, T. Otomo, K. Mori, M. Sugiyama, H. Kato, M. Hasegawa, A. Hirata, Y. Hirotsu, A.C. Hannon, Intermetallics 14 (2006) 893.

[30] A. Hirata, P. Guan, T. Fujita, Y. Hirotsu, A. Inoue, A.R. Yavari, T. Sakurai, M. Chen, Nat. Mater. 10 (2010) 28.
[31] M. Ghidelli, S. Gravier, J.-J. Blandin, T. Pardoen, J.-P. Raskin, F. Mompiou, J. Alloys Compd. 615 (2014) S348.
[32] M. Ghidelli, A. Volland, J.-J. Blandin, T. Pardoen, J.-P. Raskin, F. Mompiou, P. Djemia, S. Gravier, J. Alloys Compd. 615 (2014) S90.
[33] P. Djemia, F. Ganot, P. Moch, V. Branger, P. Goudeau, J. Appl. Phys. 90 (2001) 756.
[34] A. Kueny, M. Grimsditch, Phys. Rev. B Condens. Matter 26 (1982) 4699.
[35] W.C. Oliver, G.M. Pharr, J. Mater. Res. 19 (2003) 3.
[36] D. Pan, A. Inoue, T. Sakurai, M.W. Chen, Proc. Natl. Acad. Sci. U.S.A. 105 (2008) 14769.
[37] N.V. Steenberge, J. Sort, A. Concustell, J. Das, S. Scudino, S. Suriñach, J. Eckert, M.D. Baró, Scr. Mater. 56 (2007) 605.
[38] R. Vaidyanathan, M. Dao, G. Ravichandran, S. Suresh, Acta Mater. 49 (2001) 3781.
[39] D. Ma, A.D. Stoica, X.L. Wang, Nat. Mater. 8 (2009) 30.
[40] R. Ristić, M. Stubičar, E. Babić, Philos. Mag. 87 (2007) 5629.
[41] S.V. Madge, D.V. Louzguine-Luzgin, J.J. Lewandowski, A.L. Greer, Acta Mater. 60 (2012) 4800.
[42] Z.F. Zhang, H. Zhang, X.F. Pan, J. Das, J. Eckert, Philos. Mag. Lett. 85 (2005) 513.
[43] W.L. Johnson, K. Samwer, Phys. Rev. Lett. 95 (2005) 195501.
[44] C.A. Schuh, T.G. Nieh, Acta Mater. 51 (2003) 87.
[45] W.H. Wang, Prog. Mater. Sci. 57 (2012) 487.
[46] X.K. Xi, D.Q. Zhao, M.X. Pan, W.H. Wang, Y. Wu, J.J. Lewandowski, Phys. Rev. Lett. 94 (2005) 125510.
[47] J.J. Lewandowski, W.H. Wang, A.L. Greer, Philos. Mag. Lett. 85 (2005) 77.
[48] I. Bakonyi, Acta Mater. 53 (2005) 2509.
[49] D. Tonnies, R. Maass, C.A. Volkert, Adv. Mater 26 (2014) 5715.